

Relativistic Magnetohydrodynamic Simulations of Giant Magnetar Bursts

KOUSHIK CHATTERJEE ^{1,2,3} ALEXANDER PHILIPPOV ^{1,2} ANDREI M. BELOBORODOV ^{4,5} KYLE PARFREY ⁶
BART RIPPERDA ^{3,7,8,9} AND ELIAS R. MOST ^{10,11}

¹*Department of Physics, University of Maryland, 7901 Regents Drive, College Park, MD 20742, USA*

²*Institute for Research in Electronics and Applied Physics, University of Maryland, College Park, MD 20742, USA*

³*Canadian Institute for Theoretical Astrophysics, 60 St. George Street, Toronto, ON M5S 3H8, Canada*

⁴*Physics Department and Columbia Astrophysics Laboratory, Columbia University, 538 West 120th Street, New York, NY 10027*

⁵*Max Planck Institute for Astrophysics, Karl-Schwarzschild-Str. 1, D-85741, Garching, Germany*

⁶*Princeton Plasma Physics Laboratory, Princeton, NJ 08540, USA*

⁷*Department of Physics, University of Toronto, 60 St. George Street, Toronto, ON M5S 1A7, Canada*

⁸*David A. Dunlap Department of Astronomy, University of Toronto, 50 St. George Street, Toronto, ON M5S 3H4, Canada*

⁹*Perimeter Institute for Theoretical Physics, 31 Caroline St. North, Waterloo, ON N2L 2Y5, Canada*

¹⁰*TAPIR, Mailcode 350-17, California Institute of Technology, Pasadena, CA 91125, USA*

¹¹*Walter Burke Institute for Theoretical Physics, California Institute of Technology, Pasadena, CA 91125, USA*

(Received February 23, 2026; Revised February 23, 2026; Accepted February 23, 2026)

ABSTRACT

Gradual crustal deformation can generate strongly twisted magnetic fields around magnetars, potentially triggering giant flares with total energies exceeding 10^{44} erg. In this Letter, we present the first relativistic magnetohydrodynamic simulation of a surface shear-driven magnetar eruption, capturing reconnection-driven plasma heating, the ejection of relativistically hot plasma, and the formation of a hot fireball confined within the inner magnetosphere. We find that magnetic reconnection in the equatorial current sheet launches a hot trailing outflow capable of powering the initial spike observed in giant flares, while simultaneously leaving behind a thermally stratified fireball with sufficient thermal energy to produce the pulsating, decaying tail. Together, these features provide a self-consistent physical framework for understanding the observed energetics of magnetar giant flares. The eruption also expels a magnetically dominated giant plasmoid carrying up to $\sim 9\%$ of the magnetosphere's total magnetic energy. Furthermore, our simulation demonstrates how the plasmoid drives the formation of a blast wave—an important ingredient in models linking magnetar eruptions to fast radio bursts.

Keywords: Magnetars (992) — Magnetohydrodynamical simulations (1966) — Plasma Astrophysics (1261) — X-ray bursts (1814) — Radio transient sources (2008)

1. INTRODUCTION

Magnetars are young neutron stars with magnetic fields exceeding 10^{14} G and rotation periods of several seconds (R. C. Duncan & C. Thompson 1992). They reveal themselves through sporadic high-energy activity, the most dramatic of which are *giant flares* (for a review, see V. M. Kaspi & A. M. Beloborodov 2017). To date, three confirmed giant flares have been detected: in 1979 from the soft gamma repeater (SGR) 0526–66 (W. D. Evans et al. 1980), in 1998 from SGR 1900+14 (K. Hurley et al. 1999), and in 2004 from SGR 1806–

20 (K. Hurley et al. 2005). Each event began with an intense, sub-second spike of hard X-rays and gamma rays, followed by a tail of softer X-rays modulated by the magnetar's rotation period. Magnetars have also been closely linked to fast radio bursts (FRBs), with the Galactic magnetar SGR 1935+2154 exhibiting coincident X-ray flaring and FRB emission (C. D. Bochenek et al. 2020; CHIME/FRB Collaboration et al. 2020; S. Mereghetti et al. 2020).

The energy source for magnetar bursting activity is believed to be the evolution of the star's internal magnetic field, which induces stresses in the crust, leading to surface motions and the twisting of magnetospheric field lines. The twisting motion may occur rapidly, generat-

ing Alfvén and fast magnetosonic waves that propagate into the magnetosphere (Y. Yuan et al. 2020; L. Burnaz et al. 2025), or proceed slowly, storing magnetic energy until it is released in a sudden, violent eruption (K. Parfrey et al. 2012).

In this *Letter*, we focus on the latter scenario. Models of slowly twisted magnetospheres in the framework of force-free electrodynamics (FFE) have shown that both axisymmetric and fully three-dimensional twists can drive eruptive behavior when the total twist angle exceeds a critical threshold $\psi_{\text{crit}} \gtrsim \pi$ (D. A. Uzdensky 2002; K. Parfrey et al. 2013; F. Carrasco et al. 2019; J. F. Mahlmann et al. 2023). Although FFE simulations successfully show that a significant fraction of the magnetic twist energy, $\mathcal{E}_{\text{twist}}$, can be released during such eruptions, the method is unable to track the dissipated energy deposited as heat into the plasma, which is crucial for understanding the observed emission. The problem requires the full framework of relativistic magnetohydrodynamics (MHD) that self-consistently evolves both the electromagnetic fields and the plasma.

In this *Letter*, we present the first relativistic MHD simulation of a magnetar giant flare, focusing on the structure, evolution and energetics of the flaring magnetosphere. Our axisymmetric simulation shows how magnetic reconnection launches ultrarelativistic magnetized ejecta and loads the inner closed magnetosphere with hot plasma, creating a trapped “fireball”. We measure the basic parameters of the flare, including the partitioning of the released energy between the trapped fireball and the ejecta, thermal and electromagnetic, which are expected to power the gamma-ray flare and a possible FRB.

2. NUMERICAL METHODS

The initial unperturbed magnetosphere at time $t = 0$ is set up as a static dipolar magnetic field anchored to the star of radius r_* . The magnetic field strength is determined by a chosen field B_* at the magnetic poles of the star. The total energy of the dipole magnetosphere is

$$\mathcal{E}_{\text{dip}} \approx 3 \times 10^{47} \left(\frac{B_*}{10^{15} \text{ G}} \right)^2 \left(\frac{r_*}{10 \text{ km}} \right)^3 \text{ erg}. \quad (1)$$

The initial magnetosphere is filled with a static plasma of rest-mass density ρ and a small pressure p . It has a uniform cold-plasma magnetization parameter $\sigma_{\text{cold}} \equiv b^2/4\pi\rho c^2 = 500$ and plasma-beta parameter $\beta \equiv 8\pi p/b^2 = 10^{-8}$, where $b^2/8\pi$ is the magnetic energy density measured in the rest-frame of the MHD fluid. Here, $b^2 = b^\mu b_\mu$ where b^μ is the contravariant four-vector constructed using the fluid four-velocity u^μ , the electromagnetic field tensor $F^{\mu\nu}$, and the Levi-Civita

tensor:

$$b^\mu \equiv \frac{1}{2} \epsilon^{\mu\nu\kappa\lambda} u_\nu F_{\lambda\kappa}. \quad (2)$$

At time $t > 0$, the magnetosphere is gradually twisted by driving an axisymmetric shear motion of its foot-points on the star. We prescribe a shear profile similar to K. Parfrey et al. (2013) and J. F. Mahlmann et al. (2023):

$$\omega(\theta) = \frac{\omega_0 \sin[(\theta - \theta_C)(\pi/\theta_T)]}{1 + \exp[\kappa(|\theta - \theta_C| - \theta_T)]}, \quad (3)$$

where the sine factor provides surface velocities that change direction across $\theta = \theta_C$, thereby producing a shear twist. Our fiducial simulation places the twist center at co-latitude $\theta_C = 45^\circ$ and adopts a fall-off factor $\kappa = 50$ in the sheared stripe of angular half-width $\theta_T = 0.05\pi$.¹ The twisting rate is controlled by the parameter ω_0 . It is linearly ramped up from zero to $\omega_0 = 0.04 c/r_*$ at the beginning of the simulation and then held constant until the magnetic reconnection flare is triggered at time t_{rec} ; we ramp-down ω_0 at t_{rec} . The chosen value of ω_0 is sufficiently small to weakly affect the total twist energy at the eruption onset, while remaining large enough to mitigate losses of the magnetospheric twist due to numerical diffusion (J. F. Mahlmann et al. 2023).

The plasma is strongly heated during the magnetospheric flare, and the plasma equation of state becomes important in the heated regions. We adopt an equation of state that relates the fluid pressure p to the internal energy density U as $p = (\Gamma_{\text{ad}} - 1)U$, with an adiabatic index $\Gamma_{\text{ad}} = 4/3$. This choice is appropriate for the radiation-dominated electron-positron plasma produced in the reconnection region. The plasma is assumed to be optically thick, so that radiation diffusion can be neglected over the duration of the simulation, $t \sim 25$ ms. As a result, the generated heat is trapped and advected with the plasma.

The evolving and erupting magnetosphere also has cold regions, which are not heated by magnetic reconnection. In these regions, the FFE approximation would be adequate and useful, as it helps avoid spurious heating that appears in MHD simulations at very low plasma- β and high magnetization σ_{cold} . We maintain stable FFE-like conditions in these regions by enforcing a pressure floor and a density floor, which correspond to a minimum $\beta = 10^{-8}$ and a maximum $\sigma_{\text{cold}} = 500$.

The floors ensure that the cold plasma remains magnetically dominated, while plasma heated by magnetic

¹ We also explore alternative twist locations to investigate their impact on the eruption dynamics, see Appendix B.

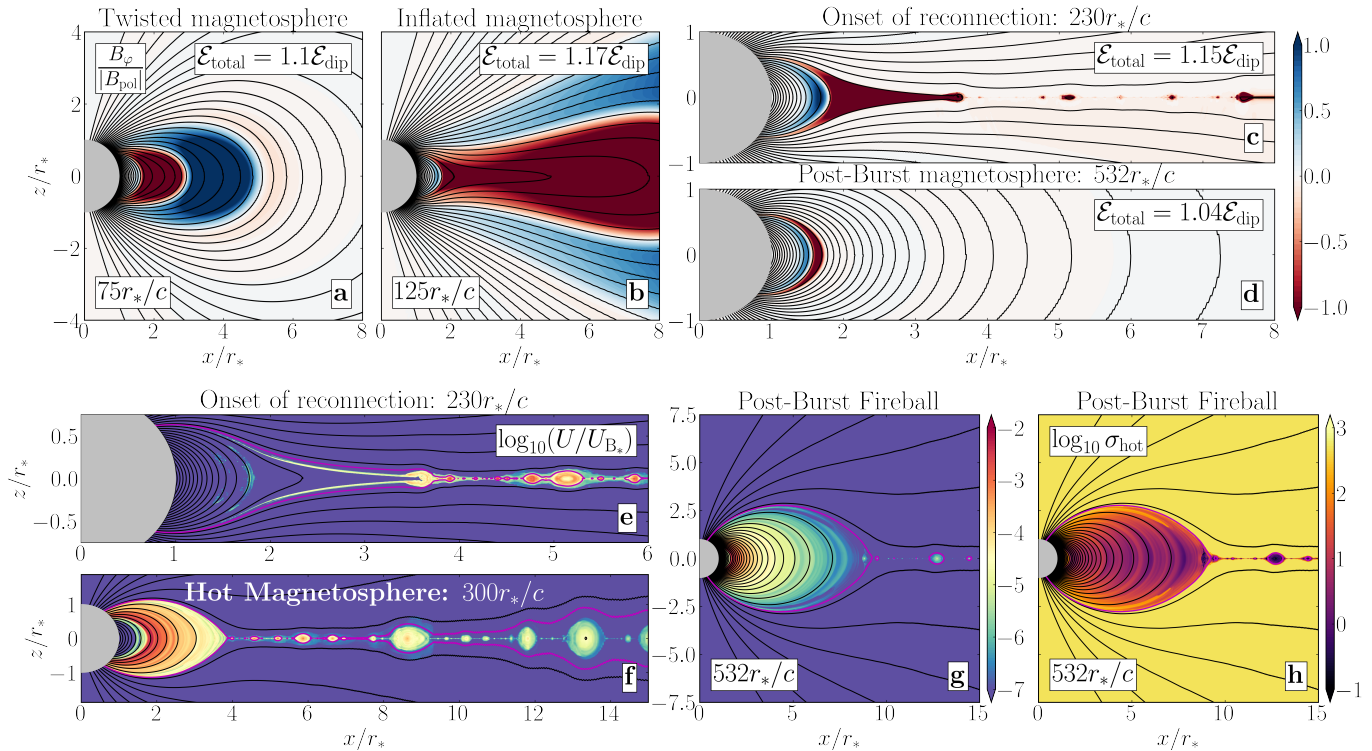


Figure 1. Onset and evolution of the eruption. *Top row (a–d):* Evolution of the inner magnetosphere ($r \leq 30r_*$) during a flare, showing the toroidal-to-poloidal magnetic energy ratio and the total magnetic energy. The magnetosphere initially inflates as the rotating stellar surface twists the magnetic field lines (a–b). Following magnetic reconnection in the equatorial plane (c), the magnetosphere relaxes toward a nearly dipolar configuration, retaining only a small residual toroidal field (d). *Bottom row (e–g):* Time evolution of the plasma internal energy, U , in the inner magnetosphere, illustrating the formation of a hot, magnetized fireball. The internal energy is normalized to the magnetic energy density $U_{B_*} = B_*^2/8\pi$ corresponding to the stellar magnetic field B_* (Eq. 1); the magenta line marks the reconnecting field line. The hot magnetization σ_{hot} (panel h) remains above unity within the fireball, indicating that the magnetosphere remains magnetically dominated.

reconnection is evolved using the full MHD equations without any floor treatment (see Appendix A for details).² The numerical stability and accuracy of the simulation is also improved by suppressing the velocity parallel to the magnetic field for the floored cold plasma in the vicinity of the star (e.g., A. Tchekhovskoy et al. 2013). Our method is able to conserve energy in the simulation domain with error $\lesssim 0.1\% \mathcal{E}_{\text{dip}}$.

We use the GPU-accelerated code H-AMR (M. T. P. Liska et al. 2022) to solve the general relativistic (GR) MHD equations in logarithmic spherical polar coordinates $(t, \log r, \theta, \varphi)$. We adopt the Minkowski metric, neglecting gravity. Grid length scales are measured

in units of the magnetar radius, r_* , and timescales in r_*/c . Our 2D simulations use an effective resolution of 20160×20160 cells, including a single layer of mesh refinement within 15° of the equatorial plane. The computational domain extends from $r \in [1, 750]r_*$ and $\theta \in [0, \pi]$. We adopt reflective boundary conditions (BCs) at the poles and at the stellar surface, periodic BCs in the φ -direction, and outflow BCs at the outer radial boundary. We fix the radial magnetic field B^r at the surface to be constant, and extrapolate the magnetic field components into the star (i.e., the ghost zone cells) as $(B^r, B^\theta, B^\varphi) \propto (r^{-3}, r^{-4}, r^{-2})$, where B^i are the contravariant field components in spherical coordinates. From hereon, we express vector components in the orthonormal basis unless otherwise stated.

3. RESULTS

The surface shear twists the dipolar magnetic field lines, generating a toroidal component (Fig. 1a) that grows as $B_\varphi \approx (\omega_0 t) B_{\text{pol}}$. At $t_{\text{inf}} \approx 120r_*/c$, the initially dipolar poloidal structure of the magnetosphere

² Our hybrid FFE–MHD implementation follows two complementary approaches: (i) during the pre-burst phase, we evolve the energy equation and impose floor values on the magnetization and plasma- β (K. Parfrey & A. Tchekhovskoy 2017, 2024); and (ii) during the flare and post-burst phases, we select the primitive-variable recovery method—either entropy inversion (S. C. Noble et al. 2009; M. T. P. Liska et al. 2022) or energy inversion—based on local plasma conditions.

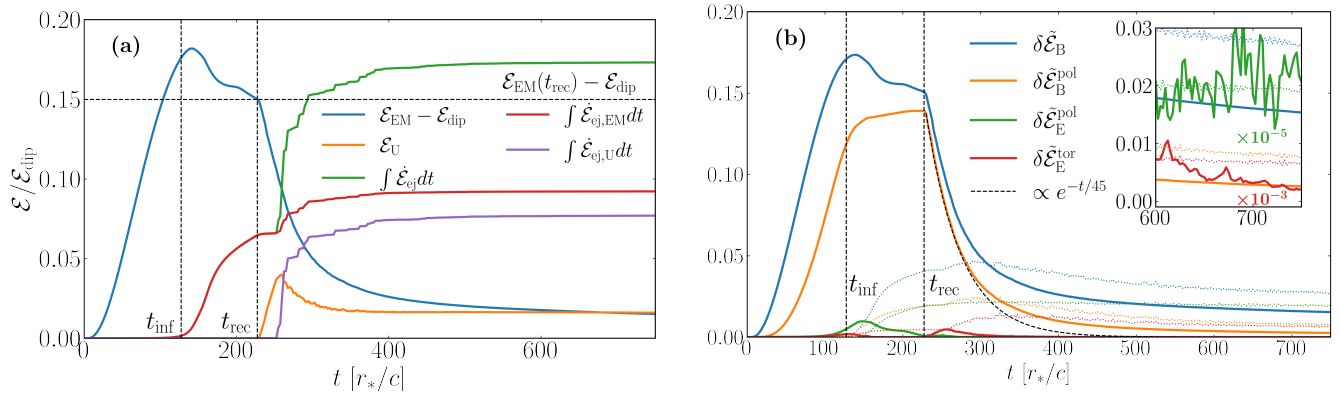


Figure 2. Flare energetics. (a) Inner magnetosphere: electromagnetic energy, \mathcal{E}_{EM} ; thermal energy, \mathcal{E}_{U} ; and the time-integrated ejected energy, $\int \dot{\mathcal{E}}_{\text{ej}} dt$, together with its individual components. We find that nearly 17% of the dipolar magnetic energy, \mathcal{E}_{dip} , is released as ejecta, powering the flare, while a substantial amount of hot plasma remains trapped in the inner magnetosphere. The horizontal dashed line denotes the twist energy stored in the inner magnetosphere at the onset of reconnection, and the vertical dashed lines mark the times of inflation and reconnection onset, respectively. (b) Decomposition of the electromagnetic energy in the inner magnetosphere (solid curves) and outside the inner region ($r > 30r_*$; dotted curves). Shown are the energies of the total and poloidal components of the magnetic field, \mathcal{E}_{B} and $\mathcal{E}_{\text{B}}^{\text{pol}}$, as well as the poloidal and toroidal electric field components, $\mathcal{E}_{\text{E}}^{\text{pol}}$ and $\mathcal{E}_{\text{E}}^{\text{tor}}$. In each case, we plot the fractional change $\delta\mathcal{E} \equiv (\mathcal{E} - \mathcal{E}_{t=0})/\mathcal{E}_{\text{dip}}$. The dashed curved line indicates an exponential fit to the decay of $\mathcal{E}_{\text{B}}^{\text{pol}}$ due to reconnection. The inset shows a zoomed-in view at late times.

begins to inflate toward a split-monopole configuration (Fig. 1b). The inflated magnetic field lines have footprints on the star at $0 < \theta \lesssim \theta_{\text{C}}$; they form the outer magnetosphere that is pushed outward by the increasing pressure $B_{\varphi}^2/8\pi$ of the twisted field lines with footprints at $\theta \sim \theta_{\text{C}}$, where surface shear is applied. We find that significant inflation occurs when the total twist angle reaches $\psi_{\text{crit}} \approx \omega_0 t_{\text{inf}} \gtrsim \pi$, consistent with previous measurements of the critical angle ψ_{crit} (e.g., J. F. Mahlmann et al. 2023).

At $t = t_{\text{rec}} \approx 215 r_*/c$, the inflated field lines become sufficiently stretched to form an equatorial current sheet and trigger magnetic reconnection (Fig. 1c). To isolate the energetics of a single ejection event, we terminate the surface twisting at the onset of reconnection in the inflated magnetosphere (continued twisting would result in repeated eruptions, see K. Parfrey et al. 2013). At $t > t_{\text{rec}}$, the outer parts of the strongly inflated field lines pinch off via magnetic reconnection while their inner parts snap back toward the star, restoring the dipolar configuration with a small residual twist (Fig. 1d). The reconnection occurs at multiple X-points in the equatorial current sheet, producing multiple hot plasmoids (Fig. 1e) which are expelled at relativistic speeds from the reconnection site. This process detaches the inflated outer magnetic loops from the star. The resulting ejecta contains a giant magnetized plasmoid composed of closed poloidal field lines filled with toroidal magnetic field (see Fig. 4).

Note that only field lines with footprints around $\theta_{\text{C}} = 45^\circ$ are strongly twisted, and field lines anchored at smaller θ are twist-free. The reconnection process first

develops in the twisted field-line bundle and later involves the twist-free field lines. During the later phase, $B_{\varphi} \approx 0$ on the reconnecting field lines, which means there is no guide field in the reconnection layer.

Some plasmoids created in the reconnection layer move inward and join the closed magnetosphere. This hot plasma descends toward the stellar surface, reflects off it, and eventually settles into a quasi-stationary layer of hot gas trapped in the closed magnetic loop (Fig. 1f). As reconnection proceeds, newly closed magnetic field lines loaded with hot plasma form successively and build up a stratified structure in which the internal energy decreases outward, forming a hot, magnetized “fireball” confined by the intense magnetic field of the magnetar (Fig. 1g). The fireball remains magnetically dominated, with a “hot magnetization” parameter $\sigma_{\text{hot}} \equiv b^2/4\pi(\rho c^2 + U + p) \gtrsim 10$ (Fig. 1h).

3.1. Flare Energetics

The total energy budget of the flare is set by the energy $\mathcal{E}_{\text{twist}}$ injected into the magnetosphere during the gradual twisting process. In general, $\mathcal{E}_{\text{twist}}$ required for eruption depends on the location and profile of the surface shear (K. Parfrey et al. 2013; J. F. Mahlmann et al. 2023). In our fiducial simulation, $\mathcal{E}_{\text{twist}} \approx 22\% \mathcal{E}_{\text{dip}}$ triggers the flare. In this subsection, we analyze how the energy stored in the inflated magnetosphere is partitioned between the energy carried by the ejecta and the residual thermal energy trapped in the closed magnetosphere.

During the time interval $t_{\text{inf}} \lesssim t \lesssim t_{\text{rec}}$, the poloidal field rapidly inflates toward a split-monopole configuration, $B_{\text{pol}} \propto r^{-2}$. We choose a sphere of radius $r = 30r_*$

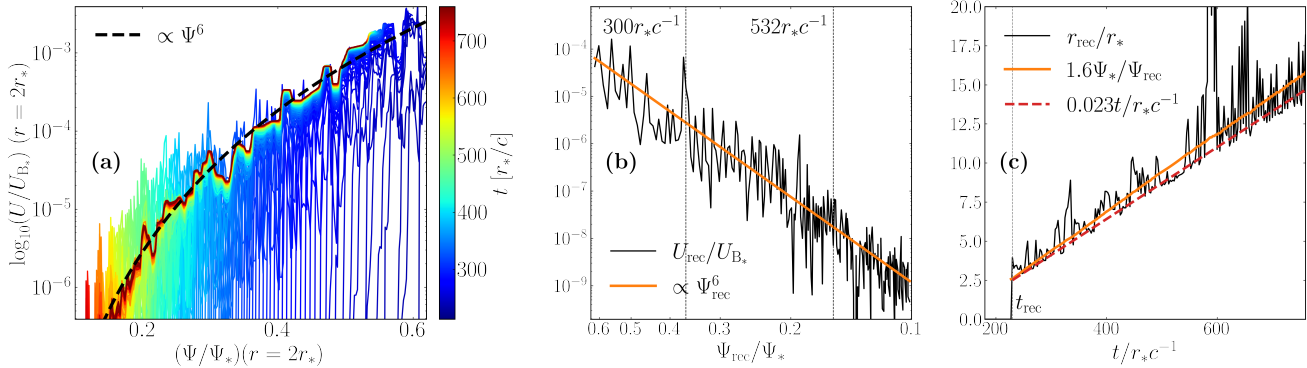


Figure 3. Time evolution of the plasma internal energy, U , and its connection to the history of reconnection. (a) Time evolution of U as a function of the poloidal flux function, Ψ , both evaluated at a fixed radius of $2r_*$. At late times, $U \propto \Psi^6$, as expected for a nearly dipolar magnetic field at the reconnection radius (see Sec. 3.2). U is normalized by U_{B_*} (see Fig. 1), and Ψ is normalized by the total stellar magnetic flux, Ψ_* . (b) Internal energy, U , as a function of the flux function evaluated at the reconnection radius, Ψ_{rec} , demonstrating $U \propto \Psi^6$, consistent with the nearly dipolar magnetic field at the reconnection radius and with panel (a). (c) Temporal evolution of the reconnection radius, r_{rec} (black curve), which migrates outward over time. Its evolution closely tracks that of $1/\Psi_{\text{rec}}$ (orange curve). A simple fit-by-eye to $r_{\text{rec}}(t)$ is overlotted, providing an estimate of the reconnection rate (see Sec. 3.2).

to measure the outflow of electromagnetic energy during the inflation and later phases. After the onset of reconnection, the magnetically dominated ejecta fully decouple from the magnetosphere and escape to infinity. Within the reconnecting current sheet, magnetic energy stored in the inflated magnetosphere is converted into thermal and kinetic energy of the plasma.

To quantify the partitioning of energy in the erupting magnetosphere, we analyze the evolution of the electromagnetic energy \mathcal{E}_{EM} and the thermal energy \mathcal{E}_{U} contained in the region $r < 30r_*$:

$$\mathcal{E}_{\text{EM,U}} = \int_{r < 30r_*} T_{\text{EM,U}}^{tt} dV, \quad (4)$$

where T_{EM} and T_{U} are the electromagnetic and thermal components of the total stress–energy tensor of the MHD, $T_{\nu}^{\mu} \equiv (\rho c^2 + U + p + b^2/4\pi)u^{\mu}u_{\nu} + (p + b^2/8\pi)\delta_{\nu}^{\mu} - b^{\mu}b_{\nu}/4\pi$, and $dV = r^2 \sin\theta dr d\theta d\varphi$ is the volume-element in spherical coordinates (t, r, θ, φ) . In addition, we decompose \mathcal{E}_{EM} into two parts, \mathcal{E}^{pol} and \mathcal{E}^{tor} , carried by the poloidal and toroidal field components. We also track the energy ejected through the sphere of radius $r = 30r_*$ by calculating the integral

$$\mathcal{E}_{\text{ej}} \equiv \int \dot{\mathcal{E}}_{\text{ej}} dt, \quad \dot{\mathcal{E}}_{\text{ej}} = \iint T_t^r r^2 \sin\theta d\theta d\varphi|_{r=30r_*}. \quad (5)$$

Figure 2 shows the evolution of the different components of the total energy remaining inside $30r_*$, as well as the energy components ejected through the sphere of $r = 30r_*$. We find that the ejecta carries away most of the twist energy, $\mathcal{E}_{\text{ej}} \approx 17.5\% \mathcal{E}_{\text{dip}} \approx 80\% \mathcal{E}_{\text{twist}}$ (Fig. 2a, green line). The ejecta energy is almost equally divided

between electromagnetic field, $\mathcal{E}_{\text{ej,EM}} \approx 9\% \mathcal{E}_{\text{dip}}$ (primarily stored in the escaping giant plasmoid), and heat, $\mathcal{E}_{\text{ej,U}} \approx 7.7\% \mathcal{E}_{\text{dip}}$ (contained in reconnection-heated plasma in the tail behind the giant plasmoid). The heated part of the ejecta can radiate the main spike of the gamma-ray flare.

Most of the magnetic twist is expelled with the ejecta. The magnetosphere inside $30r_*$ relaxes to a slightly twisted dipolar magnetosphere, with energy exceeding \mathcal{E}_{dip} by only $\sim 1\%$ (Fig. 1d, Fig. 2b).³ A large part of the closed magnetosphere ends up filled with hot plasma. The thermal energy in this trapped fireball (Fig. 2a, orange line) asymptotes to $\mathcal{E}_{\text{U}} \approx 1.5\% \mathcal{E}_{\text{dip}} \approx 6.8\% \mathcal{E}_{\text{twist}}$, which is sufficient to power the post-peak emission tail modulated with the magnetar’s rotation period (C. Thompson & R. C. Duncan 1995). FFE simulations previously estimated that the energy dissipated during an eruption is $\mathcal{E}_{\text{U,total}} \approx 10\% \mathcal{E}_{\text{twist}}$ (K. Parfrey et al. 2013), with an estimated upper bound of $\mathcal{E}_{\text{U,total}} \lesssim 25\% \mathcal{E}_{\text{twist}}$ (J. F. Mahlmann et al. 2023). We find that the total thermal energy production in our MHD simulation is $\mathcal{E}_{\text{U,total}} = \mathcal{E}_{\text{U,fireball}} + \mathcal{E}_{\text{ej,U}} = (7.7\% + 1.5\%) \mathcal{E}_{\text{dip}} \approx 42\% \mathcal{E}_{\text{twist}}$, considerably larger than the FFE dissipation estimates.

³ Once the magnetosphere has been cleared of the hot plasma and radiation generated by the flare, resistive dissipation of the residual toroidal magnetic field can sustain the quiescent X-ray emission of the magnetar (A. M. Beloborodov & C. Thompson 2007).

3.2. Formation of the Stratified Fireball

It is convenient to label magnetic field lines using the poloidal magnetic flux function, $\Psi(r, \theta) = \int_0^{2\pi} \int_0^\theta B^r r^2 \sin \theta d\theta d\varphi$, since the field lines of an axisymmetric magnetosphere lie on surfaces of constant Ψ . In the evolving magnetosphere (with magnetic field footpoints frozen into the static star), each magnetic flux surface retains the value of Ψ that it had in the initial dipole configuration. In particular, $\Psi = 0$ on the magnetic axis (which extends to infinity), and Ψ increases for field lines that close progressively closer to the star, from the pole toward the equator.

Heat in the trapped fireball is generated by magnetic reconnection, so the fireball occupies flux surfaces $\Psi_{\text{rec}} < \Psi < \Psi_1$ that have passed through the reconnection layer. Thermal energy is first deposited on the flux surfaces that reconnect earliest, at $\Psi_1 \approx 0.62 \Psi_*$, where $\Psi_* = (1/2) \int_{r=r_*} |B^r| r^2 \sin \theta d\theta d\varphi$ is the total stellar magnetic flux. Heat is added layer by layer as reconnection proceeds to $\Psi_{\text{rec}}(t) < \Psi_1$. This process produces a stratified fireball characterized by a thermal pressure $p(\Psi)$ and a thermal energy density $U = 3p$, both of which are approximately uniform on each closed flux surface Ψ , as the fireball relaxes to pressure equilibrium (Fig. 3a).

One can see the reconnecting flux surfaces in Fig. 1(e–g) in representative time snapshots. Reconnection involves tearing (X-points) of the current sheet and creates closed contours of Ψ , i.e. flux surfaces of toroidal shape, enclosing plasmoids (Fig. 1e). At each time t , we define $\Psi_{\text{rec}}(t)$ as the flux surface passing through the X-point closest to the star. The radial position of this closest point r_{rec} defines *reconnection radius* (e.g., see midplane region at $r \sim 4r_*$ in Fig. 1e). Radius $r_{\text{rec}}(t)$ represents the evolving radial extension of the reconnected magnetosphere, and $\Psi = \Psi_{\text{rec}}(t)$ defines the evolving outer boundary of the trapped fireball. We also measure the thermal energy density $U_{\text{rec}}(t)$ at point $r_{\text{rec}}(t)$; it represents the energy density being deposited into the fireball.

The simulation shows how new layers are added to the trapped fireball and how $r_{\text{rec}}(t)$ moves outward while $\Psi_{\text{rec}}(t)$ and $U_{\text{rec}}(t)$ decrease with time (Fig. 3b,c). The magnetosphere at $r < r_{\text{rec}}$ is approximately dipolar which gives $\Psi_{\text{rec}} \propto r_{\text{rec}}^{-1}$ and $B_{\text{rec}} \propto r_{\text{rec}}^{-3}$. As a result, the energy density generated by reconnection at the boundary radius r_{rec} scales as $U_{\text{rec}} \propto B_{\text{rec}}^2 \propto r_{\text{rec}}^{-6} \propto \Psi_{\text{rec}}^6$. This estimate is consistent with the evolution of U_{rec} observed in the simulation, as shown in Fig. 3a, and explains the steep stratification of thermal energy density in the trapped fireball, $U(\Psi)$.

The trapped fireball grows in size at the rate at which reconnection proceeds in the current sheet. The

reconnection rate v_{rec} in highly magnetized plasmas ranges from $\sim 0.01c$ in collisional MHD fluids to $\sim 0.1c$ in collisionless plasmas (e.g., A. Bransgrove et al. 2021). Here we estimate v_{rec} using three complementary methods. First, we infer v_{rec} from the decay timescale τ_{rec} of the poloidal magnetic energy shown in Fig. 2(b). The poloidal magnetic energy decays as $\delta \mathcal{E}_{\text{B}}^{\text{pol}} \propto e^{-t/(45r_*/c)} = (e^{-t/\tau_{\text{rec}}})^2$, which implies $\tau_{\text{rec}} \approx 2 \times 45 r_*/c = 90 r_*/c$. The initial reconnection episode occurs at an average radius $\langle r_{\text{rec}} \rangle \approx 3.5 r_*$, yielding a reconnection rate $v_{\text{rec}} \simeq \langle r_{\text{rec}} \rangle / \tau_{\text{rec}} \approx 0.038c$. Second, using the time evolution of r_{rec} (Fig. 3c), we obtain a conservative lower bound $v_{\text{rec}} \gtrsim \delta r_{\text{rec}} / \delta t \approx 0.023c$. Finally, we directly measure the inflow speed of the upstream plasma into the current sheet by sampling the vertical velocity v_z a few grid cells above the current sheet at multiple radii. After averaging over time, radius, and altitude, we find $v_{\text{rec}} \approx 0.03c$. Overall, the measured reconnection rates are consistent with those reported in previous (GR)MHD simulations, which typically find $v_{\text{rec}} \approx 0.01c$ – $0.03c$ (B. Ripperda et al. 2020; A. Bransgrove et al. 2021; M. P. Grehan et al. 2025).

3.3. Magnetic Flare Ejecta

Following the onset of reconnection, the magnetosphere ejects a giant magnetized plasmoid⁴(see, e.g., A. M. Beloborodov 2009; K. Parfrey et al. 2013). Field lines in the plasmoid were initially connected to the stellar twisting region prior to reconnection, so the plasmoid is B_φ -dominated (Fig. 4a; e.g., K. Parfrey et al. 2013; M. V. Barkov et al. 2022; J. F. Mahlmann et al. 2023). It remains cold (Fig. 4b) and flies outward at nearly the speed of light. It acts as a piston on the outer (untwisted) magnetosphere, driving a near-spherical envelope of compressed outer magnetospheric field lines, and forms a relativistically moving magnetic pulse or blast wave (Fig. 4c; A. M. Beloborodov 2020; Y. Lyubarsky 2020). The tail of the ejecta is continuously fed by the hot plasma from the reconnecting current sheet (Fig. 4b).

Prior to the onset of reconnection ($t \leq t_{\text{rec}}$), we evolve the cold plasma in the inflating outflow under enforced force-free conditions (see Appendix A), maintaining a fixed cold magnetization of $\sigma_{\text{cold}} = 500$. During this pre-reconnection phase, the leading edge of the inflated region accelerates linearly, reaching Lorentz factors of $\gamma \sim 5$. Since the ejecta are expected to transition to a

⁴ We find that the radial width of the accelerating plasmoid, Δ_w , remains approximately constant while its transverse size, Δ_\perp , grows due to sideways expansion $\Delta_\perp \propto r$. This evolution is consistent with energy conservation, $\mathcal{E}_{\text{ej}} \sim r^2 \Delta_w B^2$, and magnetic flux conservation, $\Phi \sim r \Delta_w B$.

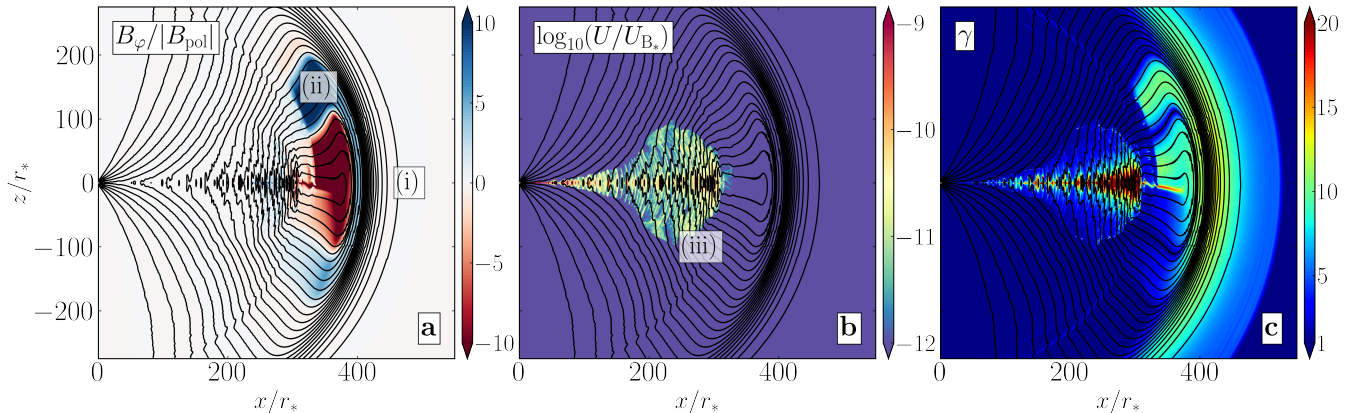


Figure 4. Structure of the flare ejecta at $532r_*/c$. Three distinct regions emerge: (i) the magnetic pulse, a relativistically moving, near-spherical envelope of compressed outer magnetospheric field lines filled with cold plasma and containing negligible toroidal field; (ii) the piston, a relativistically moving ejecta head containing cold plasma and significant toroidal magnetic fields; and (iii) the ejecta tail, filled with relativistically hot plasma moving at high Lorentz factor, which can produce the initial hard X-ray spike observed in magnetar giant flares. (a) Ratio of toroidal to poloidal magnetic field components, highlighting the dominance of B_φ in the piston. (b) Internal energy, U , normalized by the stellar magnetic energy density U_{B_*} , showing the hot plasma in the ejecta tail. (c) Lorentz factor, γ , of the different ejecta components.

slow-acceleration regime once their velocity approaches the fast magnetosonic speed (e.g., A. Tchekhovskoy et al. 2009), for $t \geq t_{\text{rec}}$ we remove the magnetization floor in the ejecta region to capture the acceleration process correctly.

Post reconnection onset, we observe the ejecta to linearly accelerate to $\gamma \sim 14$. This behavior can be understood by assuming conservation of the specific energy flux in the radial direction,

$$\sigma_0 \equiv -\frac{T_t^r}{\rho u^r} \approx \gamma(\sigma_{\text{cold}} + h + 1) \approx \gamma\sigma_{\text{cold}}, \quad (6)$$

where $\sigma_{\text{cold}} = b^2/4\pi\rho c^2$ and the gas enthalpy is $h = (U + p)/\rho$. Here we have a highly magnetized and cold plasma, i.e., $\sigma_{\text{cold}} \gg 1$ and $h \ll 1$. The ejecta is launched with a total specific energy flux $\sigma_0 \approx \gamma\sigma_{\text{cold}} \approx 2500$, and it linearly accelerates until it reaches the fast-magnetosonic speed, $\gamma = \gamma_{\text{F}} = \sigma_{\text{cold,F}}^{1/2}$. Assuming conservation of the specific energy flux, we have

$$\sigma_0 \approx \gamma_{\text{F}} \sigma_{\text{cold,F}} \approx \gamma_{\text{F}}^3, \quad (7)$$

which gives $\gamma_{\text{F}} \approx \sigma_0^{1/3} \approx 14$. The magnetization correspondingly drops to $\sigma_{\text{cold,F}} \approx \sigma_0^{2/3} \approx 200$, consistent with the numerical results. Beyond $\gamma \simeq \gamma_{\text{F}}$, the ejecta transitions to the slow-acceleration regime, which is analytically predicted to follow $\gamma \propto r^{1/3}$ (J. Granot et al. 2011). At larger distances from the magnetar, the magnetic pulse may either collide with the magnetospheric current sheet beyond the light cylinder, or drive a shock in the magnetar wind, both of which are plausible FRB production mechanisms (A. M. Beloborodov 2020; Y. Lyubarsky 2020, 2021; J. F. Mahlmann et al. 2022).

3.4. Alfvén and Fast Wave production in flares

The inflation of the magnetosphere and the subsequent onset of reconnection generate Alfvén waves (AWs). Their trapping and dissipation in the inner closed magnetosphere may provide additional heat contributing to the fireball energy and its observed radiation. We estimate the energy in AWs by approximating it as twice the energy of the poloidal electric field, $\mathcal{E}_A \approx 2\mathcal{E}_E^{\text{pol}}$. The AW energy stored within the inner magnetosphere turns out to be minuscule, $\mathcal{E}_A \ll 1\% E_{\text{dip}}$. The AWs are continuously erased by grid-scale dissipation as they progressively shear during propagation along closed magnetic field lines.

Collisions between plasmoids generated in the reconnection layer and their bombardment of the closed-field region produce compressive disturbances that launch fast magnetosonic waves (FWs), which show up in the simulation as waves of the toroidal electric field (Fig. 5). These waves propagate roughly isotropically, and are most prominent during the early reconnection phase, $230 \lesssim t/(r_*c^{-1}) \lesssim 300$. Dissipation of FWs, for example through shock formation (A. M. Beloborodov 2023), could contribute additional energy release. However, similar to AWs, their energy content remains very low, $\ll 1\% E_{\text{dip}}$. Over time, plasmoid collisions weaken and FWs escape the magnetosphere, causing a decline in FW energy within the inner region. By the end of the simulation, the remaining FW energy is $\mathcal{E}_F \sim 2\mathcal{E}_E^{\text{tor}} \lesssim 10^{-6}\mathcal{E}_{\text{dip}}$ (Fig. 2b).

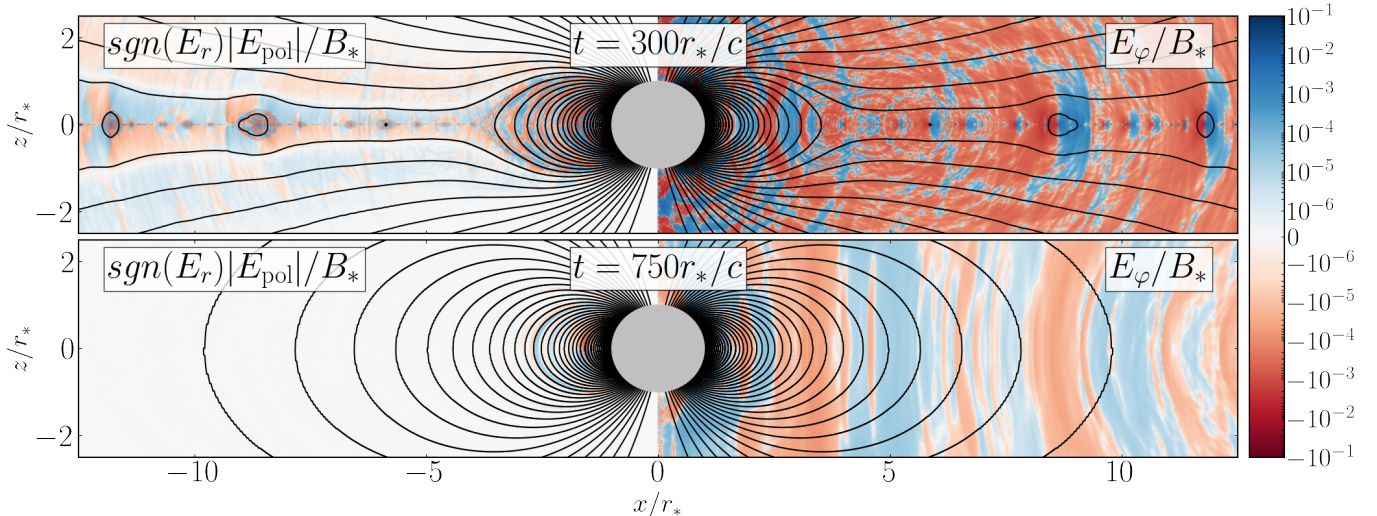


Figure 5. Production of Alfvén and fast waves during the eruption. We show electric field components shortly after the onset of reconnection (*top*) and in the post-flare state (*bottom*). The poloidal component, E_{pol} , traces Alfvén waves, while the toroidal component, E_{φ} , tracks fast magnetosonic waves. As the field lines in the inner magnetosphere close following the eruption, fast waves gradually escape the magnetosphere, whereas Alfvén waves remain confined to the inner region. The electric fields are normalized by the stellar magnetic field strength B_* .

4. DISCUSSION

In this Letter, we present the first relativistic MHD simulations of an erupting magnetar magnetosphere triggered by crustal shearing of magnetic fields anchored to the stellar surface, motivated by the three giant flares observed to date (W. D. Evans et al. 1980; K. Hurley et al. 1999, 2005). Our results show that a substantial fraction of the magnetar’s dipole energy can be released in a magnetically dominated giant plasmoid, whose trailing, hot relativistic plasma could produce the main spike of the gamma-ray flare. The eruption leaves behind hot plasma trapped in the closed magnetosphere. This trapped fireball serves as the energy reservoir powering the extended X-ray emission tail of the flare. Our simulation also demonstrates that the ejecta launches a powerful compressive wave (a fast magnetosonic pulse). This pulse carries sufficient energy to generate FRBs through its interaction with the magnetar wind (A. M. Beloborodov 2020) or the magnetospheric current sheet (Y. Lyubarsky 2020; J. F. Mahlmann et al. 2022).

4.1. Energetics and beaming

For the chosen twist profile, our simulations predict that the total thermal energy carried by the ejecta tail is $\approx 7.7\% \mathcal{E}_{\text{dip}}$, while the energy stored in the fireball is $\approx 1.5\% \mathcal{E}_{\text{dip}}$. These efficiencies set the overall energy budgets for the main spike and the extended tail of the flare. The simulations further show that the hot plasma in the ejecta tail moves relativistically ($\gamma \gtrsim 20$) and is predominantly confined to a narrow solid angle, with an angular width of $\sim 20^\circ$ (Fig. 6), along the equatorial

current sheet. The resulting strong beaming can substantially enhance the apparent luminosity of the initial spike when viewed along the ejection direction, implying that the true released energy may be considerably smaller than its isotropic-equivalent estimate.

Assuming that the giant flare is observed along the ejection direction, the measurement in Fig. 6 implies $(d\dot{\mathcal{E}}/d\Omega)_{\text{max}} \sim 0.1 \mathcal{E}_{\text{dip}}/\tau_{\text{rec}}$, and the corresponding isotropic-equivalent thermal energy of the ejecta is

$$\begin{aligned} \mathcal{E}_{\text{U, iso}}^{\text{max}} &\approx 4\pi \left(\frac{d\dot{\mathcal{E}}}{d\Omega} \right)_{\text{max}} \times \tau_{\text{rec}} \\ &\approx 3.8 \times 10^{47} \text{ erg} \left(\frac{B_*}{10^{15} \text{ G}} \right)^2, \end{aligned} \quad (8)$$

where we used Eq. 1 for estimating \mathcal{E}_{dip} for a magnetar of radius $r_* = 10 \text{ km}$. An offset of the line of sight from the ejection directions leads to substantially lower isotropic-equivalent luminosities, by factors of 10^{-1} – 10^{-3} .

Unlike the ejecta, the trapped fireball is quasi-static and its emission is not beamed. Thus, observers with any lines of sight will see a similar total radiation energy emitted by the fireball, $\approx 1.5\% \mathcal{E}_{\text{dip}} \approx 4.5 \times 10^{45} \text{ erg} (B_*/10^{15} \text{ G})^2$. The fireball energy will be reduced for flares triggered by twists located closer to the magnetic poles (see Appendix B), or for non-axisymmetric twists covering a smaller fraction of the stellar surface. Note that even axisymmetric fireballs will be observed as pulsating if the rotation axis is misaligned with the magnetic axis (since the fireball shape

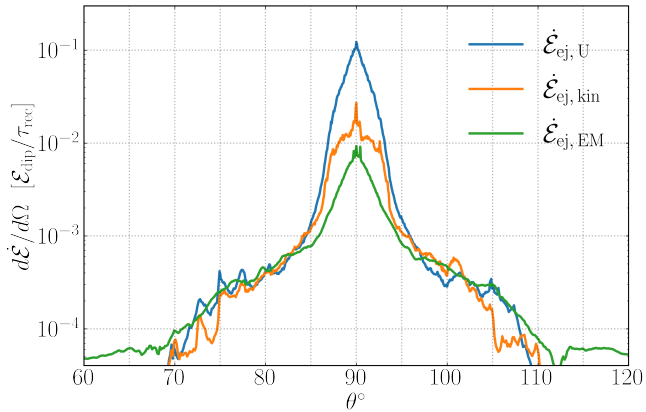


Figure 6. Angular distributions of the thermal, kinetic, and electromagnetic energy fluxes in the ejecta tail per unit solid angle, $d\dot{\mathcal{E}}/d\Omega$, are shown in units of $\mathcal{E}_{\text{dip}}/\tau_{\text{rec}}$. These quantities are averaged over 20 cells at a radius of $\sim 250 r_*$ where the tail is widest at $t = 532 r_*/c$ (see Fig. 4). In the ejecta tail, the thermal and kinetic energy fluxes dominate over the electromagnetic flux. In our model, the narrow angular extent of the tail implies non-trivial beaming-factor corrections that must be applied when inferring the intrinsic luminosity of the flare spike from observations.

and its radiation are not spherically symmetric). Fully three-dimensional simulations will be required to study more general geometries and non-axisymmetric dynamics such as kink-like instabilities in twisted flux tubes, as seen in previous FFE simulations (J. F. Mahlmann et al. 2023).

An intriguing possibility is the observation of an “orphan” pulsating tail emitted by the fireball, without an initial bright spike. This can happen if the line of sight is far from the directions of the thermal ejecta. Future work should refine estimates of the detection probability for the main spike. We expect that magnetar rotation and a more chaotic outflow from the current sheet, arising from three-dimensional effects in reconnection, may lead to a larger opening angle of the thermal ejecta. This would increase the probability of observation of the main spike compared to our axisymmetric model.

4.2. Comparison with observed giant flares

The three observed giant flares share a common two-phase structure but differ markedly in energy. Each begins with an extremely bright initial spike lasting ~ 0.2 – 0.5 seconds, followed by a softer, pulsating tail of ~ 200 – 400 seconds. The 1979 SGR 0526–66 and 1998 SGR 1900+14 events were broadly similar in scale: their initial spikes released $\sim 10^{44}$ – 10^{45} erg (isotropic equivalent), and their tails carried $\sim 10^{44}$ erg (e.g., M. Feroci et al. 2001; S. Mereghetti 2008). By contrast, the most recent giant flare detected in 2004 from SGR 1806–20 was exceptionally energetic: the isotropic-equivalent en-

ergy of its initial spike exceeded $\sim 10^{46}$ erg, nearly two orders of magnitude larger than in previous events, while its duration was comparable to that of the earlier flares. The total energy in the pulsating tails of all three flares was comparable, at $\sim 10^{44}$ erg.

The total thermal energy stored in the fireball in our simulations exceeds the energy release inferred from the pulsating tails of observed giant flares. This discrepancy likely has a geometrical origin, as discussed in Sect. 4.1; for example, the twisted region may lie closer to the magnetic poles, or it may occupy a smaller fraction of the surface than assumed in our axisymmetric model.

The large differences in isotropic-equivalent energy release for the main spikes of the three flares can be explained by the beaming effects. This suggests that the 2004 event produced ejecta closer to the line of sight compared to the other two giant flares.⁵ It is also possible that the 2004 flare was powered by a different physical mechanism altogether. A. Bransgrove et al. (2025) have recently proposed a new mechanism of “crustal eruption” — ejection of a magnetic loop from the star itself, as a result of ambipolar diffusion in its interior. This scenario can explain the observed presence of baryonic ejecta (B. M. Gaensler et al. 2005; J. Granot et al. 2006), whereas our magnetospheric eruption model naturally produces an ultra-relativistic baryon-free outflow.

4.3. Duration of the main spike

The characteristic dynamical timescale of the flare in our simulations is set by the reconnection time,

$$\tau_{\text{rec}} \approx \frac{r_{\text{rec}}}{v_{\text{rec}}} \approx 10 \text{ ms} \left(\frac{r_{\text{rec}}}{10 r_*} \right) \left(\frac{0.03}{v_{\text{rec}}/c} \right), \quad (9)$$

which is considerably shorter than the observed duration of the main spike, ~ 250 – 500 ms. Although the hot ejecta tail requires a few $\times \tau_{\text{rec}}$ to traverse a surface at $\sim 100 r_*$, our simulated flare remains significantly shorter. Positioning the twist region closer to the magnetic pole could partially increase the reconnection timescale, $\propto r_{\text{rec}} \sim r_C$, where r_C is the equatorial radius of the twisted field line. However, this would also reduce the amount of released energy, which scales approximately as $r_C^{-5/2}$, as discussed in Appendix B.

Considerable uncertainty arises in the determination of the reconnection rate in flares occurring close to the magnetar. In particular, reconnection is expected to proceed in a deeply radiative regime, where copious

⁵ This is in some tension with the non-detection of an FRB from the 2004 flare (S. P. Tendulkar et al. 2016). It suggests either a failed FRB or a missed FRB that was emitted with stronger beaming compared to the gamma-rays.

pair creation during reconnection produces an optically thick, collisional plasma (D. A. Uzdensky 2011; A. M. Beloborodov 2021). Reconnection in this regime can be influenced by the strong radiation pressure that develops around the layer, potentially reducing the reconnection rate. The details of this process are unknown and remain to be clarified using first-principles radiative simulations.

ACKNOWLEDGMENTS

This work was supported by NASA grant 80NSSC22K1054 (KC and AP), Simons Foundation (00001470, AP and BR), and facilitated by Multimessenger Plasma Physics Center (MPPC, AP and AMB), NSF grant No. PHY-2206607. A.P. additionally acknowledges support by an Alfred P. Sloan Fellowship, and a Packard Foundation Fellowship in Science and Engineering. AMB and ERM acknowledge support from NASA’s ATP program under grant 80NSSC24K1229. AMB is also supported by NSF grant AST-2408199 and Simons Foundation award 446228. ERM acknowledges support by the National

Science Foundation under grants No. PHY-2309210 and AST-2307394. BR is supported by the Natural Sciences & Engineering Research Council of Canada (NSERC) [funding reference number 568580], and the Canadian Space Agency (23JWGO2A01). This research was supported in part by grant NSF PHY-2309135 to the Kavli Institute for Theoretical Physics (KITP). KP acknowledges support from the Laboratory Directed Research and Development Program at Princeton Plasma Physics Laboratory, a national laboratory operated by Princeton University for the U.S. Department of Energy under Prime Contract No. DE-AC02-09CH11466.

This research is part of the Frontera computing project (D. Stanzione et al. 2020) at the Texas Advanced Computing Center (LRAC-AST21006). Frontera is made possible by NSF award OAC-1818253. Part of the simulations were performed on DOE OLCF Summit under allocations AST198. This research used resources of the Oak Ridge Leadership Computing Facility at the Oak Ridge National Laboratory, which is supported by the Office of Science of the U.S. Department of Energy under Contract No. DE-AC05-00OR22725.

APPENDIX

A. METHODOLOGY FOR HYBRID FFE-MHD EVOLUTION

We evolve the ideal MHD equations throughout the domain and impose force-free (FF) conditions where appropriate by enforcing thresholds on the magnetization and plasma- β , and by suppressing the fluid velocity along the magnetic field ($v_{\parallel} = 0$ close to the star), following K. Parfrey & A. Tchekhovskoy (2017, 2024). Coupling between the FF and MHD regions is achieved through a controlled buffer zone evolved with the entropy equation, as discussed below. This hybrid FF–MHD treatment yields behavior consistent with approaches that explicitly evolve the FF equations rather than enforcing floors (A. Chael 2024; S. S. Komissarov & D. Phillips 2025). Furthermore our high grid resolution ensures that we obtain converged plasmoid-mediated reconnection rates similar to resolved resistive MHD simulations due to the small numerical resistivity in the asymptotic regime in our ideal MHD simulations (M. P. Grehan et al. 2025).

To stably evolve the magnetospheric twist, reconnection in the current sheet, and the acceleration of the ejecta, we adopt a region-dependent primitive-variable recovery strategy, switching between the energy and entropy evolution equations in our GRMHD code `H-AMR` (M. T. P. Liska et al. 2022). Standard GRMHD schemes conserve total energy and impose density and pressure floors in highly magnetized regions, such as relativistic jets. In the initial phase of the twist buildup, the magnetosphere is strongly magnetically dominated. We therefore employ energy inversion throughout the domain, applying a density floor that maintains a fixed cold magnetization of $\sigma_{\text{cold}} = 500$ and an internal-energy floor that enforces $\beta \approx 10^{-8}$, effectively approximating force-free conditions. This approach ensures that the large reservoir of electromagnetic energy generated by twist injection is evolved self-consistently. The energy-inversion method becomes unreliable when the internal energy is extremely small, because it is obtained as the difference between the conserved total energy and the electromagnetic energy. When these two large quantities nearly cancel, truncation errors can yield unphysical values, including negative pressures. To avoid this, we tie the density and internal-energy floors explicitly to the local magnetic-field strength. In addition, near the star, we suppress the velocity component parallel to the magnetic field, v_{\parallel} , to prevent gas accumulation along field lines as the magnetosphere inflates, $t \gtrsim t_{\text{inf}}$.

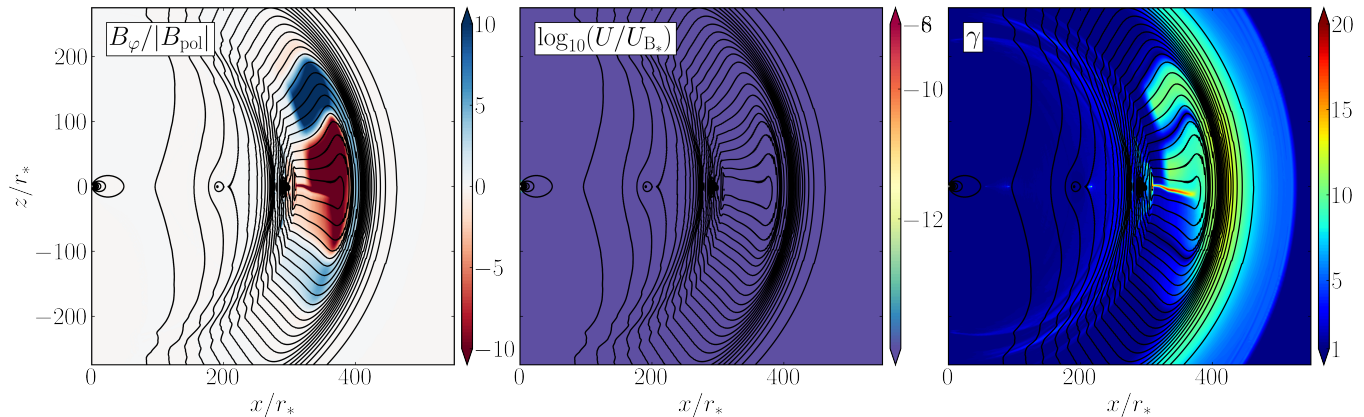


Figure 7. The same as Fig. 4, but evolved using a force-free prescription. We find that our MHD simulation accurately captures the dynamics and magnetic-field distribution of the ejecta head and the magnetic pulse when compared to the floored FFE version of the simulation. The FFE-only simulation does not capture reconnection-heating as expected.

A different strategy is required once reconnection begins and during the subsequent post-reconnection evolution, $t \gtrsim t_{\text{rec}}$. To determine where and when reconnection first occurs, we perform a simulation at the same resolution as the fiducial run but enforcing our force-free condition throughout the domain and over the entire eruption evolution. In this setup, during reconnection, thermal energy is continually reset to its floor value, causing the current sheet to lose pressure support and the domain to lose energy over time. Nevertheless, the model accurately captures the reconnection onset time, the current-sheet geometry, and the large-scale ejecta morphology. As shown in Fig. 7, the overall ejecta structure closely matches that of the fiducial run, apart from the absence of hot plasmoids. Importantly, because the ejecta head and the forward-compressed pulse remains cold and accelerates, the floored FFE simulation provides a robust estimate of the plasma acceleration before it reaches the fast-magnetosonic speed.

Guided by our force-free results, we activate a hybrid primitive-variable recovery strategy at $t = t_{\text{rec}}$, switching between energy- and entropy-inversion depending on the plasma conditions. We partition the simulation domain into four regions: (i) the equatorial reconnection layer and trailing ejecta tail, which contain hot relativistic plasma; (ii) the ejecta head, consisting of cold, accelerating gas; (iii) the fireball, containing quasi-steady hot plasma; and (iv) the inflated magnetosphere, containing sub-relativistic cold gas threaded by non-twisted magnetic fields.

The hot equatorial ejecta, where magnetic dissipation produces relativistic temperatures and strong pressure gradients, are evolved using the energy equation without applying floors, enabling accurate tracking of thermal-energy generation and bulk acceleration. The ejecta head is also evolved with the energy equation but retains only internal-energy floors, allowing its magnetization to decrease steadily as it accelerates. Removing the magnetization floor is essential: the acceleration naturally slows as the flow approaches the fast-magnetosonic limit, analogous to the behavior of relativistic jets (Sec. 3.3). In contrast, the FFE-only model artificially maintains high magnetization and therefore produces continuous linear acceleration beyond the expected fast-speed limit.

The fireball and the inflated magnetosphere are evolved using the entropy equation. Alongside total-energy conservation, H-AMR evolves the entropy equation $\nabla_{\mu}(\kappa\rho u^{\mu}) = 0$, where the specific entropy is given by $s = (\Gamma_{\text{ad}} - 1) \log \kappa$. This entropy variable is used as a backup primitive-recovery method (S. C. Noble et al. 2009) when the standard inversion fails, typically in highly magnetized regions (K. Chatterjee et al. 2019). The entropy-inversion method yields a lower estimate of the internal energy, which is subdominant to the magnetic energy in these regions, discounting any heating due to reconnection or shocks. Previous studies have shown that entropy switching performs well for problems involving magnetized flows, including spherical accretion (O. Porth et al. 2017). However, the entropy scheme cannot reliably capture acceleration or reconnection heating, making it unsuitable for the current sheet and the ejecta. It does, nonetheless, accurately describe advection of magnetic fields and the transport of both hot and cold plasma, making it well suited for evolving the fireball and the cold magnetosphere while providing a controlled buffer region between the reconnecting layer and the surrounding cold plasma. The density and internal-energy floors used during the initial twist evolution are removed in these regions, but we continue to suppress v_{\parallel} in cold plasma with non-twisted magnetic fields to avoid density pile-up and to maintain the floor magnetization and plasma- β .

The choice between switching between energy and entropy evolution is made using a smooth, local switching criterion. We adopt entropy inversion when

$$f_{\text{ent}} > 0.5 \times \left[1 - \left(\frac{r_\star}{r} \right)^8 \right] + 0.48 \times (\sin \theta)^8, \quad (\text{A1})$$

where $f_{\text{ent}} := (b^2/8\pi)/(\rho c^2 + U + p + b^2/8\pi)$ quantifies magnetic dominance. The radial dependence identifies the fireball region and preserves a cold, non-twisted magnetosphere interior to it, while the strong $(\sin \theta)^8$ dependence cleanly isolates the equatorial current sheet while still allowing extended hot plasmoids to be handled by energy inversion. The ejecta region is tracked with a moving surface at $r \approx 0.98 ct$, with a correction for the location of the ejecta head at the time of onset of reconnection. We also introduce entropy inversion in a small buffer zone between the hot ejecta tail and the ejecta head to permit limited mixing without disrupting the acceleration physics.

We validated this hybrid inversion/floor scheme by confirming that the total energy inside $r \leq 30 r_\star$ is conserved with an error $\lesssim 0.1\%$ of the initial dipole energy. At larger radii, discrepancies of a few percent arise due to the difficulty of capturing dissipation accurately in the transition zone connecting the current sheet, ejecta tail, and ejecta head, as well as from dissipation in the magnetic pulse associated with limited grid resolution.

B. DEPENDENCE ON THE TWIST LOCATION

The burst luminosity and duration, $\sim \tau_{\text{rec}}$, depend on the location of the imposed twist on the stellar surface, which is not known. To quantify the dependence of the burst luminosity on the twist location, we performed three 10080² floored FFE simulations with different choices of the twist colatitude, $\theta_C = 25^\circ, 35^\circ, \text{ and } 45^\circ$, respectively. During the initial twisting phase, $\psi \lesssim 1$ rad, the injected energy is predominantly converted into the growth of the toroidal magnetic field. Following A. M. Beloborodov (2009) and K. Parfrey et al. (2013), the excess energy stored in the twisted magnetosphere can be estimated, in the small-twist limit $\psi \ll 1$, as:

$$\mathcal{E}_{\text{twist}}(t) \approx \int \frac{B_\varphi^2}{8\pi} dV = \frac{\mu}{2cr_\star} \int_0^\pi I \psi \sin(2\theta) d\theta, \quad (\text{B2})$$

where we express the magnetic moment μ in terms of the initial dipole energy, $\mathcal{E}_{\text{dip}} = \mu^2/(3r_\star^3)$. We also make use of the poloidal current, $I = (1/2)cB_\varphi r \sin \theta$, obtained via Stokes' theorem. Expressing the twist angle ψ as the azimuthal displacement of a field line, integrated along its length (see Appendix A of A. M. Beloborodov 2009), we can relate I to ψ as:

$$I = \frac{c\mu\psi(t, \theta) \sin^4 \theta}{4r_\star^2 \cos \theta}. \quad (\text{B3})$$

Replacing I and μ in Eqn. B2,

$$\mathcal{E}_{\text{twist}}(t) \approx \frac{3}{4} \mathcal{E}_{\text{dip}} \int_0^\pi \psi^2(t, \theta) \sin^5 \theta d\theta, \quad (\text{B4})$$

where the total twist angle $\psi(t, \theta) \approx \omega(\theta)t$ (Eqn. 3) in the initial spin-up phase. Assuming a thin shearing ring, $\theta_T \ll 1$, we get:

$$\mathcal{E}_{\text{twist}}^{\text{shear}}(t) \approx \frac{3}{4} \mathcal{E}_{\text{dip}} \psi^2(t) \theta_T \sin^5 \theta_C. \quad (\text{B5})$$

Using our three FFE-only simulations, we estimate the twist energies at $\psi \sim 0.5$ from Eq. B5 as $\mathcal{E}_{\text{twist}}^{\text{shear}}(\theta_C) \approx 3\% \mathcal{E}_{\text{dip}} \sin^5 \theta_C$, keeping $\theta_T = 0.05\pi$ fixed across models. For $\theta_C = (25^\circ, 35^\circ, 45^\circ)$, this yields $\mathcal{E}_{\text{twist}}^{\text{shear}} \approx (0.04\%, 0.18\%, 0.53\%) \times \mathcal{E}_{\text{dip}}$, which we compare with the corresponding values measured directly from the simulations: $(0.06\%, 0.18\%, 0.43\%) \times \mathcal{E}_{\text{dip}}$. We find that this expression provides a good approximation to the twist energy up to $\psi \sim 0.5$ rad. As expected from our analytic estimate, the twist energy decreases as the twist center moves closer to the pole (smaller θ_C). The magnetic flux function for a dipole field is $\Psi = (2\pi\mu/r) \sin^2 \theta$, and so, $\sin^2 \theta/r$ remains constant along a field line. Consequently, the twist energy scales as $\mathcal{E}_{\text{twist}}^{\text{shear}} \propto \theta_T r_C^{-5/2}$, where $r_C = r_\star/\sin^2 \theta_C$ is the equatorial radius of the field line whose footpoint is at θ_C .

For $\psi \gtrsim 1$, the magnetosphere enters the inflationary stage, with a portion of the injected energy contributing to the growth of the poloidal field (Fig. 2b). Empirically, we find that the total twist energy injected up to reconnection, $\mathcal{E}_{\text{twist}}(t_{\text{rec}})$, is approximately $40 \mathcal{E}_{\text{twist}}(\psi \sim 0.5)$ for our chosen shearing prescription. We also observe that the exact reconnection time (and thus $\mathcal{E}_{\text{twist}}$ at t_{rec}) increases slightly with grid resolution, since the equatorial magnetic field

can become increasingly monopolar before undergoing reconnection at the grid scale (which can only be avoided by introducing an explicit resistive length scale). Twists located closer to the pole produce larger twisted loops (i.e., larger r_C), trigger reconnection at greater radii, and release a smaller amount of energy, scaling approximately as $\sim \mathcal{E}_{\text{twist}} \sim r_C^{-5/2}$.

REFERENCES

- Barkov, M. V., Sharma, P., Gourgouliatos, K. N., & Lyutikov, M. 2022, *ApJ*, 934, 140, doi: [10.3847/1538-4357/ac7b80](https://doi.org/10.3847/1538-4357/ac7b80)
- Beloborodov, A. M. 2009, *ApJ*, 703, 1044, doi: [10.1088/0004-637X/703/1/1044](https://doi.org/10.1088/0004-637X/703/1/1044)
- Beloborodov, A. M. 2020, *ApJ*, 896, 142, doi: [10.3847/1538-4357/ab83eb](https://doi.org/10.3847/1538-4357/ab83eb)
- Beloborodov, A. M. 2021, *ApJ*, 921, 92, doi: [10.3847/1538-4357/ac17e7](https://doi.org/10.3847/1538-4357/ac17e7)
- Beloborodov, A. M. 2023, *ApJ*, 959, 34, doi: [10.3847/1538-4357/acf659](https://doi.org/10.3847/1538-4357/acf659)
- Beloborodov, A. M., & Thompson, C. 2007, *ApJ*, 657, 967, doi: [10.1086/508917](https://doi.org/10.1086/508917)
- Bochenek, C. D., Ravi, V., Belov, K. V., et al. 2020, *Nature*, 587, 59, doi: [10.1038/s41586-020-2872-x](https://doi.org/10.1038/s41586-020-2872-x)
- Bransgrove, A., Beloborodov, A. M., & Levin, Y. 2025, arXiv e-prints, arXiv:2508.13419. <https://arxiv.org/abs/2508.13419>
- Bransgrove, A., Ripperda, B., & Philippov, A. 2021, *PhRvL*, 127, 055101, doi: [10.1103/PhysRevLett.127.055101](https://doi.org/10.1103/PhysRevLett.127.055101)
- Burnaz, L., Most, E. R., & Bransgrove, A. 2025, arXiv e-prints, arXiv:2508.18033, doi: [10.48550/arXiv.2508.18033](https://doi.org/10.48550/arXiv.2508.18033)
- Carrasco, F., Viganò, D., Palenzuela, C., & Pons, J. A. 2019, *MNRAS*, 484, L124, doi: [10.1093/mnrasl/slz016](https://doi.org/10.1093/mnrasl/slz016)
- Chael, A. 2024, *MNRAS*, 532, 3198, doi: [10.1093/mnras/stae1692](https://doi.org/10.1093/mnras/stae1692)
- Chatterjee, K., Liska, M., Tchekhovskoy, A., & Markoff, S. B. 2019, *MNRAS*, 490, 2200, doi: [10.1093/mnras/stz2626](https://doi.org/10.1093/mnras/stz2626)
- CHIME/FRB Collaboration, Andersen, B. C., Bandura, K. M., et al. 2020, *Nature*, 587, 54, doi: [10.1038/s41586-020-2863-y](https://doi.org/10.1038/s41586-020-2863-y)
- Duncan, R. C., & Thompson, C. 1992, *ApJL*, 392, L9, doi: [10.1086/186413](https://doi.org/10.1086/186413)
- Evans, W. D., Klebesadel, R. W., Laros, J. G., et al. 1980, *ApJL*, 237, L7, doi: [10.1086/183222](https://doi.org/10.1086/183222)
- Feroci, M., Hurley, K., Duncan, R. C., & Thompson, C. 2001, *ApJ*, 549, 1021, doi: [10.1086/319441](https://doi.org/10.1086/319441)
- Gaensler, B. M., Kouveliotou, C., Gelfand, J. D., et al. 2005, *Nature*, 434, 1104, doi: [10.1038/nature03498](https://doi.org/10.1038/nature03498)
- Granot, J., Komissarov, S. S., & Spitkovsky, A. 2011, *MNRAS*, 411, 1323, doi: [10.1111/j.1365-2966.2010.17770.x](https://doi.org/10.1111/j.1365-2966.2010.17770.x)
- Granot, J., Ramirez-Ruiz, E., Taylor, G. B., et al. 2006, *ApJ*, 638, 391, doi: [10.1086/497680](https://doi.org/10.1086/497680)
- Grehan, M. P., Ghosal, T., Beattie, J. R., et al. 2025, *PhRvD*, 112, 063046, doi: [10.1103/8xf2-x2nq](https://doi.org/10.1103/8xf2-x2nq)
- Hurley, K., Cline, T., Mazets, E., et al. 1999, *Nature*, 397, 41, doi: [10.1038/16199](https://doi.org/10.1038/16199)
- Hurley, K., Boggs, S. E., Smith, D. M., et al. 2005, *Nature*, 434, 1098, doi: [10.1038/nature03519](https://doi.org/10.1038/nature03519)
- Kaspi, V. M., & Beloborodov, A. M. 2017, *ARA&A*, 55, 261, doi: [10.1146/annurev-astro-081915-023329](https://doi.org/10.1146/annurev-astro-081915-023329)
- Komissarov, S. S., & Phillips, D. 2025, *MNRAS*, 536, 1268, doi: [10.1093/mnras/stae2620](https://doi.org/10.1093/mnras/stae2620)
- Liska, M. T. P., Chatterjee, K., Issa, D., et al. 2022, *ApJS*, 263, 26, doi: [10.3847/1538-4365/ac9966](https://doi.org/10.3847/1538-4365/ac9966)
- Lyubarsky, Y. 2020, *ApJ*, 897, 1, doi: [10.3847/1538-4357/ab97b5](https://doi.org/10.3847/1538-4357/ab97b5)
- Lyubarsky, Y. 2021, *Universe*, 7, 56, doi: [10.3390/universe7030056](https://doi.org/10.3390/universe7030056)
- Mahlmann, J. F., Philippov, A. A., Levinson, A., Spitkovsky, A., & Hakobyan, H. 2022, *ApJL*, 932, L20, doi: [10.3847/2041-8213/ac7156](https://doi.org/10.3847/2041-8213/ac7156)
- Mahlmann, J. F., Philippov, A. A., Mewes, V., et al. 2023, *ApJL*, 947, L34, doi: [10.3847/2041-8213/accada](https://doi.org/10.3847/2041-8213/accada)
- Mereghetti, S. 2008, *A&A Rv*, 15, 225, doi: [10.1007/s00159-008-0011-z](https://doi.org/10.1007/s00159-008-0011-z)
- Mereghetti, S., Savchenko, V., Ferrigno, C., et al. 2020, *ApJL*, 898, L29, doi: [10.3847/2041-8213/aba2cf](https://doi.org/10.3847/2041-8213/aba2cf)
- Noble, S. C., Krolik, J. H., & Hawley, J. F. 2009, *ApJ*, 692, 411, doi: [10.1088/0004-637X/692/1/411](https://doi.org/10.1088/0004-637X/692/1/411)
- Parfrey, K., Beloborodov, A. M., & Hui, L. 2012, *ApJL*, 754, L12, doi: [10.1088/2041-8205/754/1/L12](https://doi.org/10.1088/2041-8205/754/1/L12)
- Parfrey, K., Beloborodov, A. M., & Hui, L. 2013, *ApJ*, 774, 92, doi: [10.1088/0004-637X/774/2/92](https://doi.org/10.1088/0004-637X/774/2/92)
- Parfrey, K., & Tchekhovskoy, A. 2017, *ApJL*, 851, L34, doi: [10.3847/2041-8213/aa9c85](https://doi.org/10.3847/2041-8213/aa9c85)
- Parfrey, K., & Tchekhovskoy, A. 2024, *ApJ*, 975, 57, doi: [10.3847/1538-4357/ad737b](https://doi.org/10.3847/1538-4357/ad737b)
- Porth, O., Olivares, H., Mizuno, Y., et al. 2017, *Computational Astrophysics and Cosmology*, 4, 1, doi: [10.1186/s40668-017-0020-2](https://doi.org/10.1186/s40668-017-0020-2)

- Ripperda, B., Bacchini, F., & Philippov, A. A. 2020, ApJ, 900, 100, doi: [10.3847/1538-4357/ababab](https://doi.org/10.3847/1538-4357/ababab)
- Stanzione, D., West, J., Evans, R. T., et al. 2020, in Practice and Experience in Advanced Research Computing, PEARC '20 (New York, NY, USA: Association for Computing Machinery), 106–111
- Tchekhovskoy, A., McKinney, J. C., & Narayan, R. 2009, ApJ, 699, 1789, doi: [10.1088/0004-637X/699/2/1789](https://doi.org/10.1088/0004-637X/699/2/1789)
- Tchekhovskoy, A., Spitkovsky, A., & Li, J. G. 2013, MNRAS, 435, L1, doi: [10.1093/mnrasl/slt076](https://doi.org/10.1093/mnrasl/slt076)
- Tendulkar, S. P., Kaspi, V. M., & Patel, C. 2016, ApJ, 827, 59, doi: [10.3847/0004-637X/827/1/59](https://doi.org/10.3847/0004-637X/827/1/59)
- Thompson, C., & Duncan, R. C. 1995, MNRAS, 275, 255, doi: [10.1093/mnras/275.2.255](https://doi.org/10.1093/mnras/275.2.255)
- Uzdensky, D. A. 2002, ApJ, 574, 1011, doi: [10.1086/341119](https://doi.org/10.1086/341119)
- Uzdensky, D. A. 2011, SSRv, 160, 45, doi: [10.1007/s11214-011-9744-5](https://doi.org/10.1007/s11214-011-9744-5)
- Yuan, Y., Beloborodov, A. M., Chen, A. Y., & Levin, Y. 2020, ApJL, 900, L21, doi: [10.3847/2041-8213/abafa8](https://doi.org/10.3847/2041-8213/abafa8)